

RSC Advances



This is an *Accepted Manuscript*, which has been through the Royal Society of Chemistry peer review process and has been accepted for publication.

Accepted Manuscripts are published online shortly after acceptance, before technical editing, formatting and proof reading. Using this free service, authors can make their results available to the community, in citable form, before we publish the edited article. This *Accepted Manuscript* will be replaced by the edited, formatted and paginated article as soon as this is available.

You can find more information about *Accepted Manuscripts* in the [Information for Authors](#).

Please note that technical editing may introduce minor changes to the text and/or graphics, which may alter content. The journal's standard [Terms & Conditions](#) and the [Ethical guidelines](#) still apply. In no event shall the Royal Society of Chemistry be held responsible for any errors or omissions in this *Accepted Manuscript* or any consequences arising from the use of any information it contains.

Controllable synthesis of InTaO₄ catalysts of different morphologies using a versatile sol precursor for photocatalytic evolution of H₂†

Gui-Sheng Zeng,^a Jian Yu,^a Hong-Yun Zhu,^a Hui-Long Liu,^a Qiu-Ju Xing,^a Shao-Kui Bao,^a Shun He,^a Jian-Ping Zou,^{a,*} Chak-Tong Au^b

^a Key Laboratory of Jiangxi Province for Persistent Pollutants Control and Resources Recycle, Nanchang Hangkong University, Nanchang, Jiangxi 330063, P. R. China

^b Department of Chemistry, Hong Kong Baptist University, Kowloon Tong, Hong Kong, P. R. China

ABSTRACT: For the first time, InTaO₄ photocatalysts with different morphologies and structures were facilely prepared using a versatile sol precursor. SEM, TEM and HRTEM were used to characterize their structures and morphologies. The as-synthesized materials exhibit different physicochemical properties. Compared to InTaO₄ nanoparticles and SiO₂@InTaO₄ core-shell nanospheres, InTaO₄ nanofibers is higher in light absorption ability, larger in specific surface area, and better in photocatalytic activity for hydrogen evolution. We proposed mechanisms for the formation and photocatalytic activity of the three catalysts. The present work not only provides a new approach for the synthesis of tantalates that are different in morphology and structure but also offers new insights into the controllable preparation of photocatalysts through a versatile precursor for environmental and energy applications.

Keywords: InTaO₄; Controllable synthesis; Hydrogen evolution; Photocatalyst; Water

* Corresponding author. E-mail: zjp_112@126.com (J.-P. Zou); Tel: +86 791 83863373; Fax: +86 791 83953373.

† Electronic Supplementary Information (ESI) available: See DOI: 10.1039/b000000x.

splitting

1. Introduction

It is desirable to transform solar energy to hydrogen energy by water splitting over photocatalysts [1-3]. Tantalates such as $K_2Ta_2O_6$ [4], $NaTaO_3$ [5], $BiTaO_4$ [6], Bi_3TaO_7 [7], $BaTa_2O_6$ [8], $Cd_2Ta_2O_7$ [9], and $InTaO_4$ [10] are regarded as good catalysts for the process. Among them, $InTaO_4$ is intensively studied because its band gap corresponds well with the spectrum of sunlight and the conduction band edge is more negative than the H^+/H_2 redox potential [11,12]. However, no effort was made to synthesize $InTaO_4$ that are different in morphology or structure.

It is known that the performance of a photocatalyst is highly dependent on its morphology, crystal structure, crystallinity, and particle size [13]. These are factors that directly influence the band gap structure, charge separation, transport of photogenerated carriers, and photochemical reaction [14]. To promote performance, researchers prepared anatase TiO_2 in the form of sphere, rod, wire, tube, belt and sheet as well as slightly or heavily truncated octahedron [15-17]. Furthermore, Liu et al. reported the change of photocatalytic reactivity through the tuning of facet composition [18]. As for the use of other metal oxides, Lin et al. [19] reported that compared to commercially available ZnO , coral-like ZnO nanoparticles show nearly 30% improvement in terms of quantum efficiency. And Pal et al. [20] reported that the photocatalytic activity over hierarchically assembled porous MnO_2 is much better than those over MnO_2 of other morphologies considered by them. To the best of our knowledge, the research on controllable synthesis of tantalates with different morphologies and/or structures was rarely reported [21]. For the control of morphology and structure, approaches such as adjustment of pH values, use of a surfactant as directing reagent, and control of reaction time and/or temperature during synthesis are adopted [22-24]. But there is no report on the use of a versatile sol precursor for controllable syntheses of tantalates. It is hence meaningful to develop such an approach for controllable synthesis of $InTaO_4$ species that are different in

morphology and structure.

In this article, we report for the first time the successful preparation of InTaO_4 nanoparticles, $\text{SiO}_2@ \text{InTaO}_4$ core-shell nanospheres, and InTaO_4 nanofibers using a versatile sol precursor as illustrated in Scheme 1. We studied the photocatalytic performance of them for H_2 generation from water splitting, and propose mechanisms for their formation and photocatalytic reactivity.

2. Experimental

2.1. Materials

In this study, Ta_2O_5 ($\geq 99.99\%$), $\text{In}(\text{NO}_3)_3$ ($\geq 99.99\%$), and Chloroplatinic acid hexahydrate ($\text{H}_2\text{PtCl}_6 \cdot 6\text{H}_2\text{O}$, AR, Pt $\geq 37.5\%$) were purchased from Aladdin Co., Ltd. (Shanghai, China) whereas polyvinylpyrrolidone K-30 (PVP, GR) was supplied by Sinopharm Chemical Reagent Co., Ltd. (Shanghai, China). Tetraethyl silicate (AR), triethanolamine (AR), ethylene glycol (EG, AR), ethanol (AR), hydrogen peroxide 30% (30% H_2O_2 , AR), citric acid (CA, AR), ammonia solution ($\text{NH}_3 \cdot \text{H}_2\text{O}$, AR), and HF (AR) were obtained from Guangzhou Xilong Chemical Co., Ltd. (Guangzhou, China). Water was purified using a Milli-Q water system (Bedford, USA). All chemicals were used without further purification.

2.2. Syntheses

2.2.1. Synthesis of InTaO_4 sol precursor

Ta_2O_5 (1.1015 mmol) was dissolved in HF (15 mL) at 80 °C for 10 h, and $\text{NH}_3 \cdot \text{H}_2\text{O}$ was added until a solution pH of 9. The supernatant was removed when the solution became clear, and then deionized water was added in. The procedure was repeated 3 times and finally $\text{Ta}(\text{OH})_5$ was collected by filtration. The collected $\text{Ta}(\text{OH})_5$ was dissolved in citric acid solution (8.812 mmol), and 2 mL H_2O_2 was added with stirring at 50 °C until the solution was clear. Then $\text{In}(\text{NO}_3)_3$ solution (2.203 mmol $\text{In}(\text{NO}_3)_3$ dissolved in 3mL ethylene glycol) was added at 50 °C with continued stirring for the

formation of a transparent InTaO_4 sol precursor.

2.2.2. Synthesis of InTaO_4 nanoparticles

Typically, the as-obtained InTaO_4 sol precursor was kept at 80 °C under stirring for the formation of a wet gel. The wet gel was dried at 110 °C for 10 h and then subject to calcination at 400 °C for 4 h and then at 1100 °C for 6 h to obtain the InTaO_4 nanoparticles.

2.2.3. Synthesis of $\text{SiO}_2@ \text{InTaO}_4$ core-shell nanospheres

Typically, 0.7 g SiO_2 nanospheres (prepared according to the Stöber method [25,26]) was added to the as-obtained InTaO_4 sol precursor and the mixture was stirred at 80 °C for the formation of a wet gel which was dried at 110 °C for 10 h and subject to calcination at 400 °C for 4 h and then at 1100 °C for 6 h for the generation of the $\text{SiO}_2@ \text{InTaO}_4$ core-shell nanospheres.

2.2.4. Synthesis of InTaO_4 nanofibers

The InTaO_4 nanofibers was prepared according to the electrospinning process described by Thavasi et al. [27]. Typically, polyvinylpyrrolidone was added to the as-obtained InTaO_4 sol precursor and the mixture was stirred for 2 h to reach well dispersion at a sol viscosity of 3363 mPa·S. The viscous solution was then allowed to stand for 8 h to get rid of the air bubbles. Subsequently, the viscous solution was loaded into a 10 mL plastic syringe with a metallic needle connected to a high-voltage generator. The flow rate of the viscous solution was 0.3 mL/h and the applied electric voltage was 18 kV while the humidity level inside the electrospinning chamber was around 50%. Finally, the as-spun fibers was calcined at 400 °C for 4 h and then at 1100 °C for 6 h to obtain the InTaO_4 nanofibers.

2.3. Characterization

The crystalline phases of samples were investigated by X-ray diffraction (XRD, D8 Advance, Bruker, Germany) using graphite monochromatized $\text{Cu-K}\alpha$ ($\lambda = 1.5406 \text{ \AA}$)

radiation. The XRD data for indexing and cell-parameter calculations were collected in a scan mode with scanning speed of 2°/min in the 2 θ range of 10° to 70°. UV-visible diffuse reflectance spectra (UV-vis DRS, U-3900/3900H, Hiachi High-Technologies, Japan) of powder samples in the form of dry-pressed disk were obtained using a U-3900/3900H UV-vis spectrophotometer equipped with labsphere diffuse reflectance accessory. BaSO₄ was used as reflectance standard in the UV-vis DRS studies. The photoluminescence (PL) measurements were performed on a Hitachi F-7000 spectrophotometer equipped with a 150 W xenon lamp being the excitation source. The morphologies of the products were characterized by scanning electron microscopy (SEM, Sirion 200, FEI, Holland) equipped with an energy-dispersive X-ray spectrometer (EDS). Further morphological and structural characterizations were based on transmission electron microscopy (TEM, Tecnai F20, FEI, USA) and high-resolution transmission microscopy (HRTEM). And the Brunauer-Emmett-Teller (BET) surface areas of samples were measured by means of N₂ adsorption over a NOVA 2000e (Quantachrome) equipment.

Electrochemical measurements were performed on a CHI 660D electrochemical workstation (Shanghai Chenhua, China) using a standard three-electrode cell having a working electrode, a graphite electrode as counter electrode, and a standard calomel electrode in saturated KCl (as reference electrode). The working electrodes were prepared by dip-coating: 50 mg of photocatalyst was suspended in 5 mL deionization water to produce a slurry that was then dip-coated onto a 2 cm \times 0.5 cm fluorine-tin oxide (FTO) glass electrode. The films were dried under ambient condition. The electrolyte (0.5 M Na₂SO₄) was purged with nitrogen and the other conditions were similar to those of electrochemical measurements.

2.4. Photocatalytic activity for water splitting

Photocatalytic reactions were carried out in a Pyrex top-irradiation reaction vessel (100 mL capacity) that was connected to a glass gas system. A 300 W Xe lamp (Wavelength Range: 320 nm \leq λ \leq 780 nm, Light Intensity: 160 mW/cm²) was used to generate simulated sunlight. H₂ production was achieved by dispersing 50 mg of

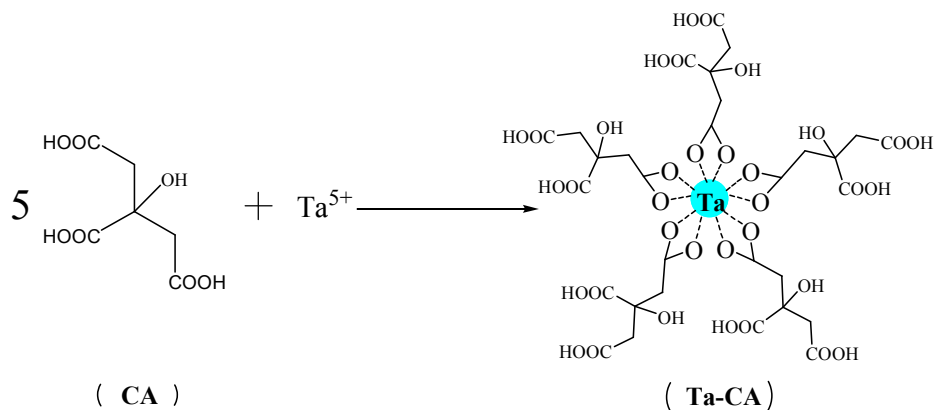
catalyst in an aqueous solution (80 mL) containing triethanolamine (10 vol.%) as sacrificial electron donor. The co-catalyst (Pt nanoparticles) was in-situ introduced by photodeposition method [28] where 3 wt% (with respect to Pt) $\text{H}_2\text{PtCl}_6 \cdot 6\text{H}_2\text{O}$ was added and well distributed in the solution. Prior to irradiation, the reaction solution was evacuated several times for complete removal of air. During the test the temperature of the reaction solution was maintained at 6 °C by a flow of cooling water. The evolved gases were analyzed by a gas chromatographic system equipped with a thermal conductive detector (TCD) and a 5Å molecular sieve column, using argon as carrier gas.

3. Results and discussion

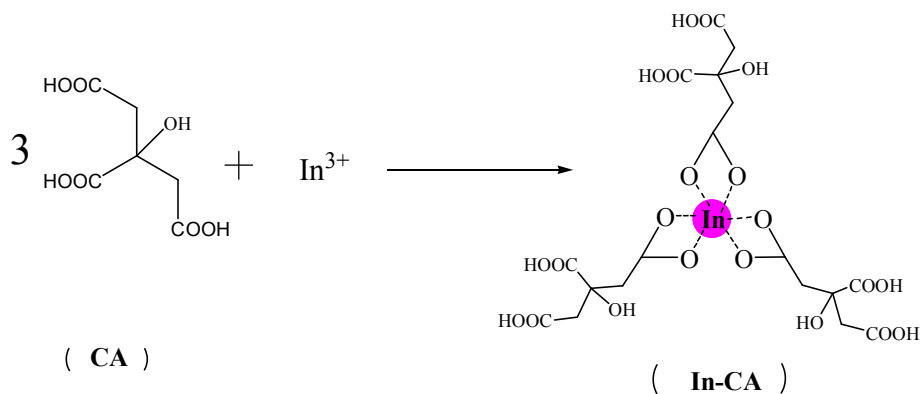
3.1. Proposed formation mechanism of the as-prepared catalysts

Scheme 1 illustrates the preparation process and formation mechanism of InTaO_4 nanoparticles, $\text{SiO}_2@\text{InTaO}_4$ core-shell nanospheres and InTaO_4 nanofibers. First, Ta_2O_5 was dissolved by hydrofluoric acid, and then the white precipitate of $\text{Ta}(\text{OH})_5$ was obtained by dropwise addition of ammonia into the above Ta_2O_5 solution. Second, $\text{Ta}(\text{OH})_5$ and $\text{In}(\text{NO}_3)_3$ solutions were mixed with citric acid (CA) solution, and Ta-CA and In-CA complexes were obtained after stirring at 50 °C for about 2 h [29]. Third, a polymeric resin (InTaO_4 sol precursor) was formed through the polyesterification of ethylene glycol (EG) with Ta-CA and In-CA [30]. The formation of InTaO_4 sol precursor was illustrated by the following equations:

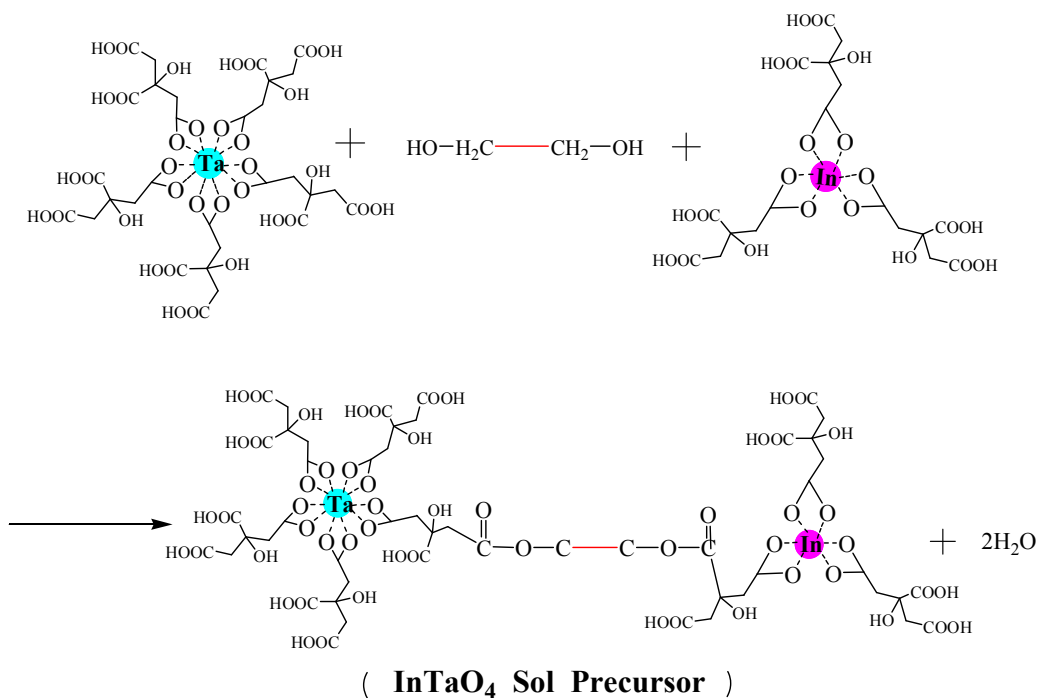
(1)



(2)



(3)



The three kinds of samples with different morphologies and structures can be prepared by using the as-synthesized InTaO₄ sol precursor. The InTaO₄ nanoparticles was obtained by annealing the InTaO₄ sol precursor while SiO₂@InTaO₄ core-shell nanospheres was obtained by annealing a mixture of the precursor and SiO₂ particles under the as-mentioned conditions. As for the InTaO₄ nanofibers, it was obtained by electrospinning the precursor followed by calcination at 1100 °C. Noteworthy, this is the first time that the polymeric resin was used as sol precursor for the synthesis of InTaO₄ species with different morphologies and structures.

3.2. Materials Characterization

The XRD patterns of InTaO₄ nanoparticles, SiO₂@InTaO₄ core-shell nanospheres, and InTaO₄ nanofibers calcined at 1100 °C for 6 h are shown in Fig. 1. The XRD patterns of the as-prepared samples can be readily indexed to monoclinic InTaO₄ (JCPDS NO. 01-081-1196). It is noted that the (1 1 0) diffraction peak of InTaO₄ at 23.13° and the center of SiO₂ broadband at 23.0°. The two peaks overlap together (See Fig. S4). But there is no change of SiO₂ and InTaO₄ crystal phases as observed over SiO₂@InTaO₄ core-shell nanospheres. In addition, the peak quality of InTaO₄ nanofibers is superior to those of InTaO₄ nanoparticles and SiO₂@InTaO₄ core-shell nanospheres, indicating high crystallinity of the InTaO₄ nanofibers. Such supremacy in crystallinity could be a reason for the higher efficiency of InTaO₄ nanofibers in the photocatalytic evolution of hydrogen as illustrated later in comparison to the InTaO₄ nanoparticles and SiO₂@InTaO₄ core-shell nanospheres.

The morphologies of the as-prepared samples were revealed by SEM. Fig. 2a shows the SEM image of the InTaO₄ nanoparticles. It can be clearly seen that the sample is composed of aggregated particles with size ranging from 200 to 800 nm. As shown in Fig. 2b, the image of SiO₂@InTaO₄ shows spheres with particle size around 400 nm that are made up of SiO₂ nanocores and InTaO₄ nanoshells. As for the as-spun InTaO₄ fibers, Fig. 2c shows fibrous images that are 0.5~2 μm in diameters while Fig. 2d shows well-crystallized nanofibers 50~200 nm in diameters. The results indicate that after calcination at 1100 °C for 6 h, the as-spun InTaO₄ fibers was successfully converted to InTaO₄ nanofibers. The EDS result further confirms the elemental composition of the as-prepared InTaO₄ (Fig. S1).

The morphological and structural features of the as-prepared samples were further examined by TEM and HRTEM. From Figs. 3a and 3b, it can be seen that InTaO₄ is coated on SiO₂ nanospheres, and the core-shell structures can be clearly observed. Furthermore, the SiO₂@InTaO₄ core-shell nanospheres are rather uniform in size with an average diameter of about 400 nm, in good agreement with the SEM image. Fig. 3c shows the InTaO₄ nanofibers is with diameters of 50~200 nm, in good agreement with the SEM image (Fig. 2d). The HRTEM image of InTaO₄ nanofibers is

shown in Fig. 3d. The fringes of $d = 0.303$ nm is ascribed to the (1 1 -1) plane of monoclinic InTaO_4 . The result demonstrates that InTaO_4 nanofibers was prepared successfully by the electrostatic spinning method. The SEM and TEM of InTaO_4 nanoparticles after photodeposition of Pt were studied. As shown in Figs. S2(a)-(f), the sizes of Pt nanoparticles rang from 4 to 20 nm. The EDS result further confirms the existence of Pt nanoparticles (Figs. S2(g)-(i)).

Fig. 4a depicts the UV-vis diffuse absorption spectra of the as-synthesized catalysts. The as-prepared InTaO_4 shows a typical semiconductor absorption in the region of 200~450 nm. According to the Kubelka-Munk method [31], the band gaps of InTaO_4 nanofibers and InTaO_4 nanoparticles were determined to be 3.17 and 3.27 eV, respectively (Fig. S3). It is found that the band gap of $\text{SiO}_2@/\text{InTaO}_4$ core-shell nanospheres is similar to that of InTaO_4 nanoparticles because the former consists of InTaO_4 and non-conductor SiO_2 . Compared with the absorption edges of InTaO_4 nanoparticles and $\text{SiO}_2@/\text{InTaO}_4$ core-shell nanospheres, that of InTaO_4 nanofibers is markedly red-shifted, suggesting that the band structure of InTaO_4 is dependent on its morphology and can be adjusted likewise. The result is consistent with the good photocatalytic activity of InTaO_4 nanofibers as shown later.

The photoluminescent properties of the photocatalysts were examined with excitation wavelength of 360 nm. As shown in Fig. 4b, the as-prepared InTaO_4 exhibits broad luminescence (410~600 nm) centered at ca. 460 nm at room temperature. The broad PL is maybe ascribed to the effect of oxygen vacancies according to the reported literatures [32-36]. The PL intensity of the InTaO_4 nanofibers is worse than those of InTaO_4 nanoparticles and $\text{SiO}_2@/\text{InTaO}_4$ core-shell nanospheres, suggesting lower electron-hole recombination rate of InTaO_4 nanofibers. Such property of the InTaO_4 nanofibers can be attributed to the efficient transportation of the photoexcited carriers at the surface, in consistent with the below photocurrent result.

Sharp photocurrent responses can be observed over the working electrodes upon pulses of Xe lamp irradiation in Fig. 5 that depicts the photocurrent-time (I-t) curves. The photocurrents are reproducible and stable during the four intermittent on-off

irradiation cycles. The prompt increase in photocurrent response from the light-off to the light-on state is ascribed to the quick separation and transportation of photogenerated electrons on the surfaces of the working electrodes. The InTaO₄ nanofibers exhibits higher photocurrent response than SiO₂@InTaO₄ core-shell nanospheres and InTaO₄ nanoparticles. The results indicate that nanofibers can effectively delay fast recombination of photogenerated carriers. The photoelectrochemical results are consistent with the better photocatalytic performance of InTaO₄ nanofibers for hydrogen evolution as illustrated below.

Table S1 shows that the BET surface area of InTaO₄ nanofibers is 4.1579 m²/g, whereas those of InTaO₄ nanoparticles and SiO₂@InTaO₄ core-shell nanospheres are 3.1405 and 2.9093 m²/g, respectively. It is generally agreed that a catalyst higher in surface area is higher in the availability of active sites. Thus, besides charge separation efficiency, being large in surface area is another reason for the high photocatalytic performance of InTaO₄ nanofibers. And the large BET value of InTaO₄ nanofibers is attributed to its unique morphology.

3.3. Photocatalytic results

The photocatalytic activities of the as-synthesized catalysts for H₂ production were evaluated under the irradiation of simulated sunlight. As shown in Fig. 6, the InTaO₄ nanofibers shows much higher activity (the hydrogen evolution efficiency is 29.92 μmol·g⁻¹·h⁻¹) than that of InTaO₄ nanoparticles and SiO₂@InTaO₄ core-shell nanospheres. According to the characterization results, the superior photocatalytic activity of InTaO₄ nanofibers is attributed to its supremacy in terms of specific surface area, crystallinity and light absorption ability.

As shown in Scheme 2, a possible mechanism was proposed to explain the photocatalytic activity of InTaO₄ nanoparticles, SiO₂@InTaO₄ core-shell nanospheres and InTaO₄ nanofibers. According to the Mott-Schottky (MS) plots of InTaO₄ nanofibers and InTaO₄ nanoparticles (Fig. S4), reversed sigmoidal plots for as-synthesized InTaO₄ were observed, which is consistent with that typical for n-type semiconductors [37,38]. The V_{fb} as calculated from the x intercepts of the linear

region are found to be -0.883 and -0.871 V vs. SCE (equivalent to -0.641 and -0.629 V vs. NHE, respectively) for InTaO₄ nanofibers and InTaO₄ nanoparticles, respectively. Hence the CB of InTaO₄ nanofibers and InTaO₄ nanoparticles can be calculated to be -0.841 and -0.829 V, respectively. According to the E_g values in Fig. S3, the VB of InTaO₄ nanofibers and InTaO₄ nanoparticles can be calculated to be 2.329 and 2.441 V, respectively. The CB and VB of SiO₂@InTaO₄ core-shell nanospheres are equal to that of InTaO₄ nanoparticles. Based on the above results, the bottom level of the conduction bands of InTaO₄ nanofibers, InTaO₄ nanoparticles, and SiO₂@InTaO₄ core-shell nanospheres are much more negative than the reduction potential of H⁺/H₂ (0 V). According to photocatalytic theory [39], with such CB potentials, the three catalysts are able to reduce water to H₂ upon excitation by an appropriate energy. Under solar irradiation, electrons (e⁻) in VB are excited to CB, with the same amount of holes (h⁺) left in the VB of photocatalyst. Then there is transfer of electrons from the CB of photocatalysts toward the Pt nanoparticles. And the Pt nanoparticles provide active sites where H⁺ is effectively reduced to H₂ by the separated electrons while the sacrificial reagent of triethanolamine is oxidized by the holes.

4. Conclusions

A new strategy was proposed for the synthesis of InTaO₄ nanoparticles, SiO₂@InTaO₄ core-shell nanospheres, and InTaO₄ nanofibers using a versatile sol precursor for H₂ evolution from water splitting. The experimental results indicate that InTaO₄ species with different morphologies and structures exhibit different physicochemical properties. Among the three, InTaO₄ nanofibers is the highest in light utilization efficiency, specific surface area, and photocatalytic activity for hydrogen evolution. A possible formation mechanism and photocatalytic mechanism were also proposed to elucidate the synthetic process of the three catalysts as well as the relation between their structures and properties. The present work provides a new approach for synthetic control of morphologies and structures of photocatalysts.

Acknowledgements

We gratefully acknowledge the financial support of the NSF of China (51238002, 51272099, 51378246, and 20801026), the NSF of Jiangxi Province (KJLD12002 and 20114BAB203005), and the Foundation of State Key Laboratory of Structural Chemistry (20100015).

Notes and references

- [1] X. B. Chen, S. H. Shen, L. J. Guo and S. S. Mao, *Chem. Rev.*, 2010, **110**, 6503-6570.
- [2] M. G. Walter, E. L. Warren, J. R. McKone, S. W. Boettcher, Q. Mi, E. A. Santori and N. S. Lewis, *Chem. Rev.*, 2010, **110**, 6446-6473.
- [3] A. Kudo and Y. Miseki, *Chem. Soc. Rev.*, 2009, **38**, 253-278.
- [4] G. Zhang, W. Jiang and S. Yu, *Mater. Res. Bull.*, 2010, **45**, 1741-1747.
- [5] W. Jiang, X. L. Jiao and D. R. Chen, *Int. J. Hydrogen Energy*, 2013, **38**, 12739-12746.
- [6] C. G. Almeida, H. M. C. Andrade, A. J. S. Mascarenhas and L. A. Silva, *Mater. Lett.*, 2010, **64**, 1088-1090.
- [7] G. Zhang, M. Li, S. Yu, S. Zhang, B. Huang and J. Yu, *J. Colloid Interf. Sci.*, 2010, **345**, 467-473.
- [8] T. G. Xu, X. Zhao and Y. F. Zhu, *J. Phys. Chem. B*, 2006, **110**, 25825-25832.
- [9] H. H. Yang, X. R. Liu, Z. H. Zhou and L. J. Guo, *Catal. Commun.*, 2013, **31**, 71-75.
- [10] Y. C. Chiou, U. Kumar and J. C. S. Wu, *Appl. Catal. A*, 2009, **357**, 73-78.
- [11] R. Ullah, H. Q. Sun, S. B. Wang, H. M. Ang and M. O. Tade, *Ind. Eng. Chem. Res.*, 2012, **51**, 1563-1569.
- [12] Z. G. Zou, J. H. Ye, K. Sayama and H. Arakawa, *Nature*, 2001, **414**, 625-627.
- [13] M. Ashokkumar, *Int. J. Hydrogen Energy*, 1998, **23**, 427-438.
- [14] J. G. Yu, Y. F. Yu, P. Zhou, W. Xiao and B. Cheng, *Appl. Catal. B*, 2014, **156-157**, 184-191.
- [15] H. G. Yang, C. H. Sun, S. Z. Qiao, J. Zou, G. Liu, S. C. Smith, H. M. Cheng and G.

- Q. Lu, *Nature*, 2008, **453**, 638-641.
- [16] E. J. W. Crossland, N. Noel, V. Sivaram, T. Leijtens, J. A. Alexander-Webber and H. J. Snaith, *Nature*, 2013, **495**, 215-219.
- [17] X. Chen and S. S. Mao, *Chem. Rev.*, 2007, **107**, 2891-2959.
- [18] G. Liu, J. C. Yu, G. Q. Lu and H. M. Cheng, *Chem. Commun.*, 2011, **47**, 6763-6783.
- [19] J. C. Lin, C. P. Lee and K. C. Ho, *J. Mater. Chem.*, 2012, **22**, 1270-1273.
- [20] P. Pal, S. K. Pahari, A. K. Giri, S. Pal, H. C. Bajaj and A. B. Panda, *J. Mater. Chem. A*, 2013, **1**, 10251-10258.
- [21] P. Wang, P. Chen, A. Kostka, R. Marschall and M. Wark, *Chem. Mater.*, 2013, **25**, 4739-4745.
- [22] K. Q. Zhou, Q. J. Zhang, Y. Q. Shi, S. H. Jiang, Y. Hu and Z. Gui, *J. Alloy. Compd.*, 2013, **577**, 389-394.
- [23] Y. H. Ao, Y. Y. Gao, P. F. Wang, C. Wang, J. Hou and J. Qian, *Mater. Res. Bull.*, 2014, **49**, 223-228.
- [24] J. P. Zou, S. L. Luo, L. Z. Zhang, J. Ma, S. L. Lei, L. S. Zhang, X. B. Luo, Y. Luo, G. S. Zeng and C. T. Au, *Appl. Catal. B*, 2013, **140-141**, 608-618.
- [25] W. Stöber and A. Fink, *J. Colloid Interf. Sci.*, 1968, **26**, 62-69.
- [26] P. Jiang, J. F. Bertone, K. S. Hwang and V. L. Colvin, *Chem. Mater.*, 1999, **11**, 2132-2140.
- [27] V. Thavasi, G. Singh and S. Ramakrishna, *Energy Environ. Sci.*, 2008, **1**, 205-221.
- [28] H. Park, W. Choi and M. R. Hoffmann, *J. Mater. Chem.*, 2008, **18**, 2379-2385.
- [29] M. Kakihana, *J. Sol-Gel. Sci. Technol.*, 1996, **6**, 7-55.
- [30] J. Lin, M. Yu, C. K. Lin and X. M. Liu, *J. Phys. Chem. C*, 2007, **111**, 5835-5845.
- [31] H. Lin, C. P. Huang, W. Li, C. Ni, S. I. Shah and Y. H. Tseng, *Appl. Catal. B*, 2006, **68**, 1-11.
- [32] X. Liu and M. T. Swihart, *Nanoscale*, 2013, **5**, 8029-8036.
- [33] C. Drouilly, J. M. Krafft, F. Averseng, S. Casale, D. Bazer-Bachi, C. Chizallet, V. Lecocq, H. Vezin, H. Lauron-Pernot and G. Costentin, *J. Phys. Chem. C*, 2012, **116**, 21297-21307.

- [34] X. S. Peng, G. W. Meng, J. Zhang, X. F. Wang, Y. W. Wang, C. Z. Wang and L. D. Zhang, *J. Mater. Chem.*, 2002, **12**, 1602-1605.
- [35] C. Liang, Guo. Meng, Y. Lei, F. Phillipp and L. Zhang, *Adv. Mater.*, 2001, **13**, 1330-1333.
- [36] H. Chang, K. Kong, Y. S. Choi, E. In, Y. Choi, J. O. Baeg and S. J. Moon, *Chem. Phys. Lett.*, 2004, **398**, 449-452.
- [37] E. Gao, W. Wang, M. Shang and J. Xu, *Phys. Chem. Chem. Phys.*, 2011, **13**, 2887-2893.
- [38] Y. Zhou, X. Zhang, Z. Zhao, Q. Zhang, F. Wang and Y. Lin, *Superlattice. Microst.*, 2014, **72**, 238-244.
- [39] O. Carp, C. L. Huisman and A. Reller, *Prog. Solid State Chem.*, 2004, **32**, 33-177.

Graphics captions

Scheme 1. Schematic illustration of the formation of InTaO₄ nanoparticles, SiO₂@InTaO₄ core-shell nanospheres, and InTaO₄ nanofibers.

Fig. 1. XRD patterns of SiO₂, SiO₂@InTaO₄ core-shell nanospheres, InTaO₄ nanoparticles, and InTaO₄ nanofibers.

Fig. 2. SEM images of (a) InTaO₄ nanoparticles, (b) SiO₂@InTaO₄ core-shell nanospheres, (c) as-spun fibers of InTaO₄, and (d) InTaO₄ nanofibers.

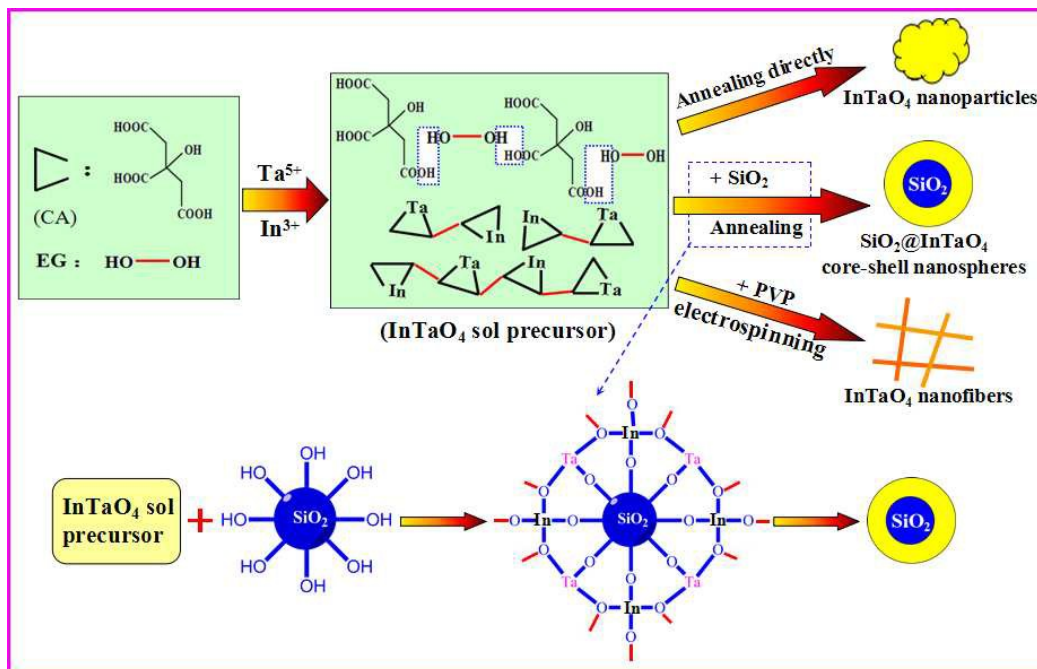
Fig. 3. TEM images of (a) InTaO₄ nanoparticles, (b) SiO₂@InTaO₄ core-shell nanospheres, and (c) InTaO₄ nanofibers; (d) HRTEM image of InTaO₄ nanofibers.

Fig. 4. (a) UV-vis absorbance spectra of InTaO₄ nanoparticles, SiO₂@InTaO₄ core-shell nanospheres, and InTaO₄ nanofibers; (b) PL spectra of InTaO₄ nanoparticles, SiO₂@InTaO₄ core-shell nanospheres, and InTaO₄ nanofibers at an excitation wavelength of 360 nm.

Fig. 5. Photocurrent responses of InTaO₄ nanoparticles, SiO₂@InTaO₄ core-shell nanospheres, and InTaO₄ nanofibers.

Fig. 6. The rate of hydrogen evolution over InTaO₄ nanoparticles, SiO₂@InTaO₄ core-shell nanospheres, and InTaO₄ nanofibers under simulated solar irradiation.

Scheme 2. Photocatalytic scheme of InTaO₄ nanoparticles, SiO₂@InTaO₄ core-shell nanospheres, and InTaO₄ nanofibers.



Scheme 1. Schematic illustration of the formation of InTaO₄ nanoparticles, SiO₂@InTaO₄ core-shell nanospheres, and InTaO₄ nanofibers.

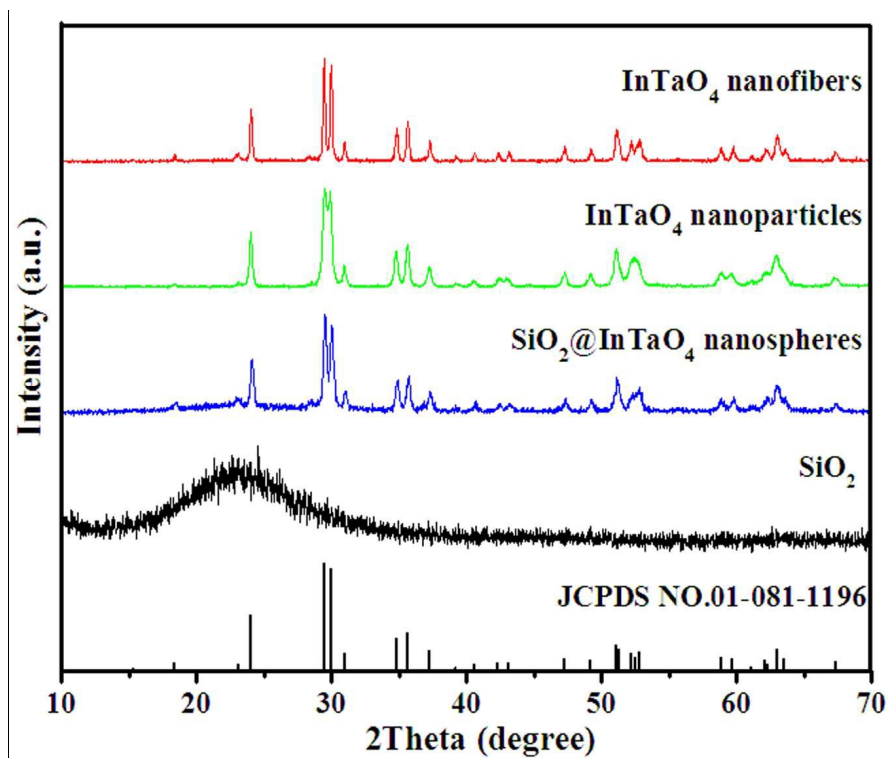


Fig. 1. XRD patterns of SiO₂, SiO₂@InTaO₄ core-shell nanospheres, InTaO₄ nanoparticles, and InTaO₄ nanofibers.

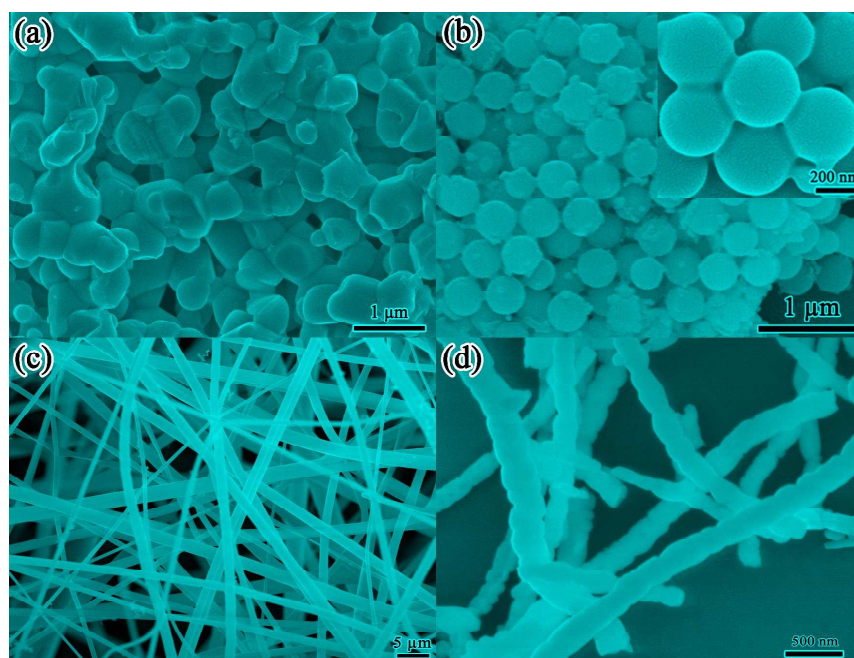


Fig. 2. SEM images of InTaO_4 nanoparticles (a), $\text{SiO}_2@ \text{InTaO}_4$ core-shell nanospheres (b), as-spun fibers of InTaO_4 (c), and InTaO_4 nanofibers (d).

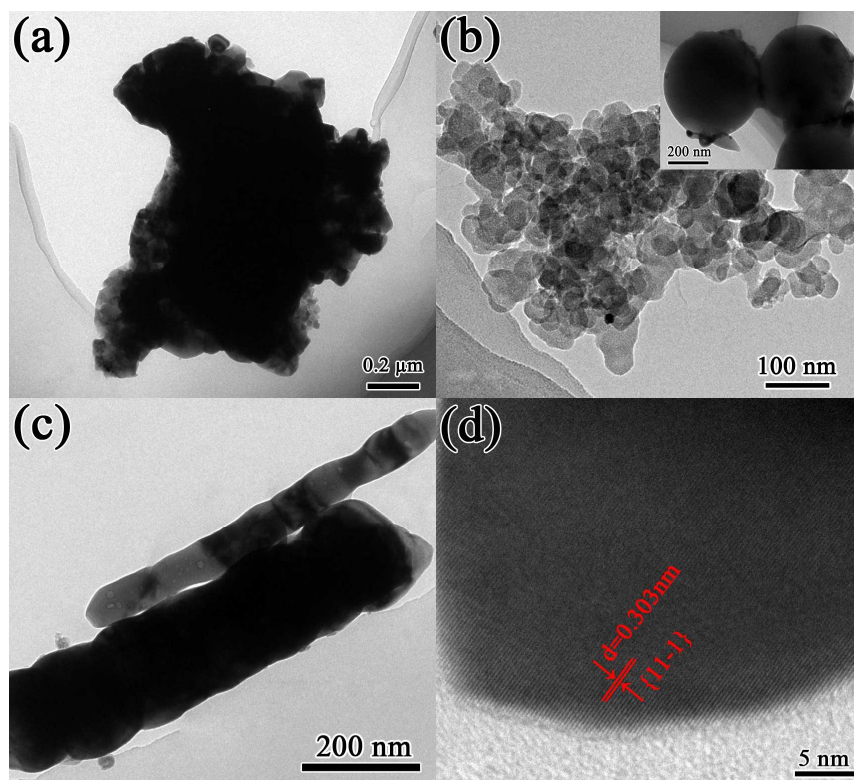


Fig. 3. TEM images of InTaO_4 nanoparticles (a), $\text{SiO}_2@ \text{InTaO}_4$ core-shell

nanospheres (b), and InTaO_4 nanofibers (c); HRTEM image of InTaO_4 nanofibers (d).

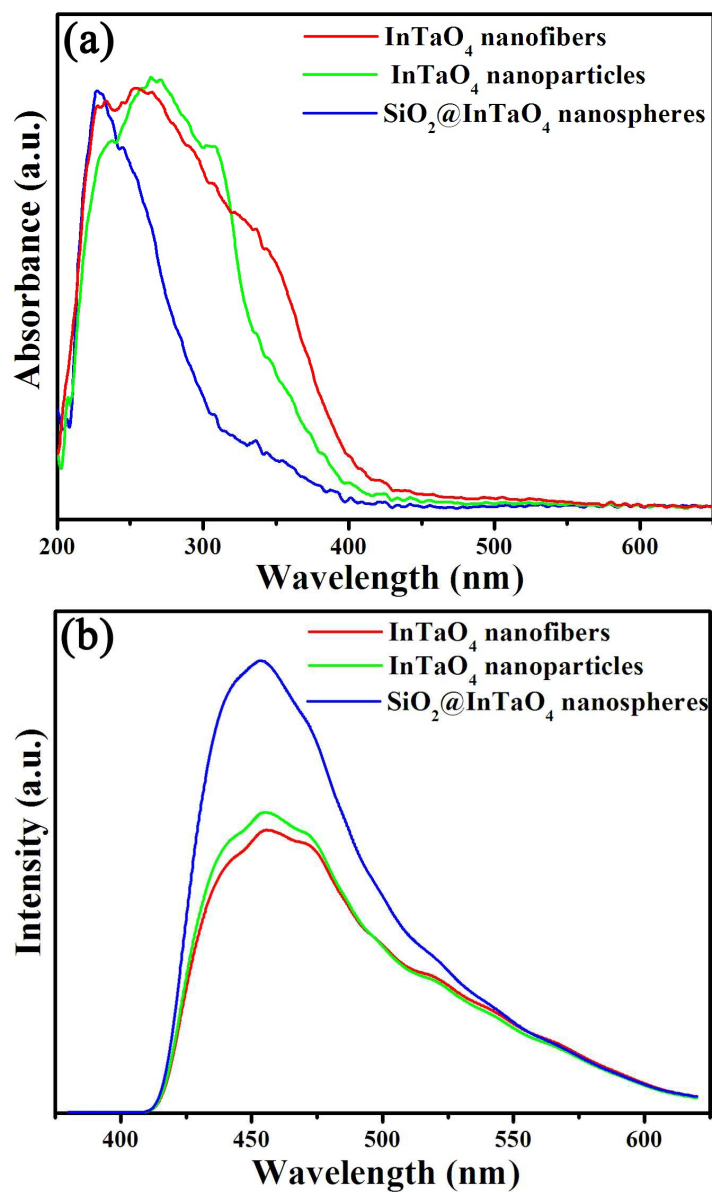


Fig. 4. (a) UV-vis absorbance spectra of InTaO_4 nanoparticles, $\text{SiO}_2@/\text{InTaO}_4$ core-shell nanospheres, and InTaO_4 nanofibers; (b) PL spectra of InTaO_4 nanoparticles, $\text{SiO}_2@/\text{InTaO}_4$ core-shell nanospheres, and InTaO_4 nanofibers at an excitation wavelength of 360 nm.

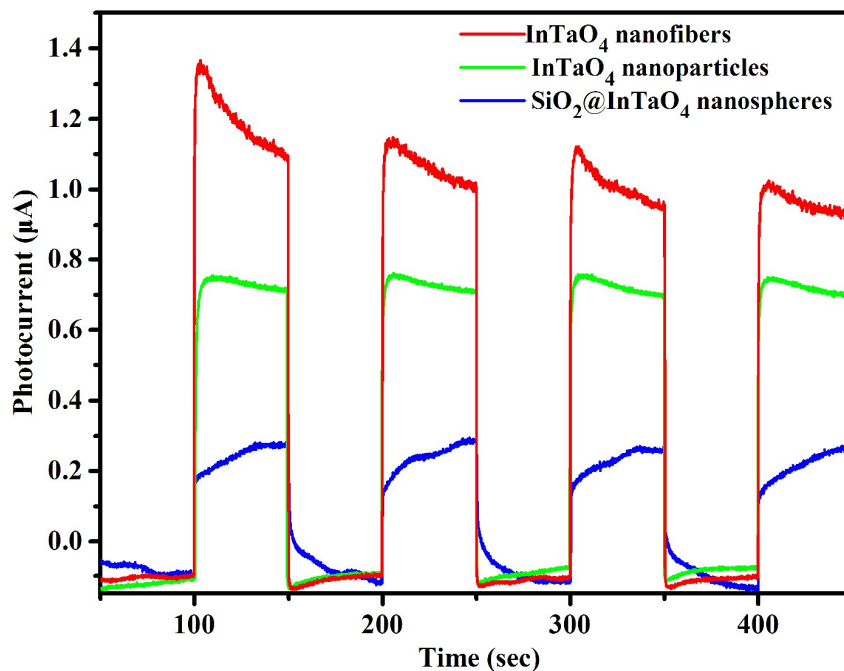


Fig. 5. Photocurrent responses of InTaO₄ nanoparticles, SiO₂@InTaO₄ core-shell nanospheres, and InTaO₄ nanofibers.

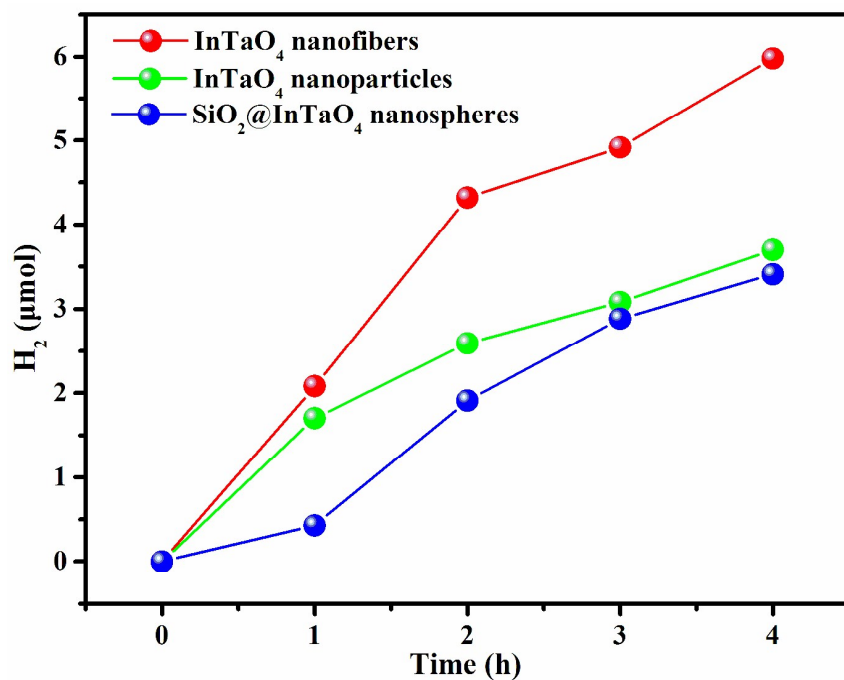
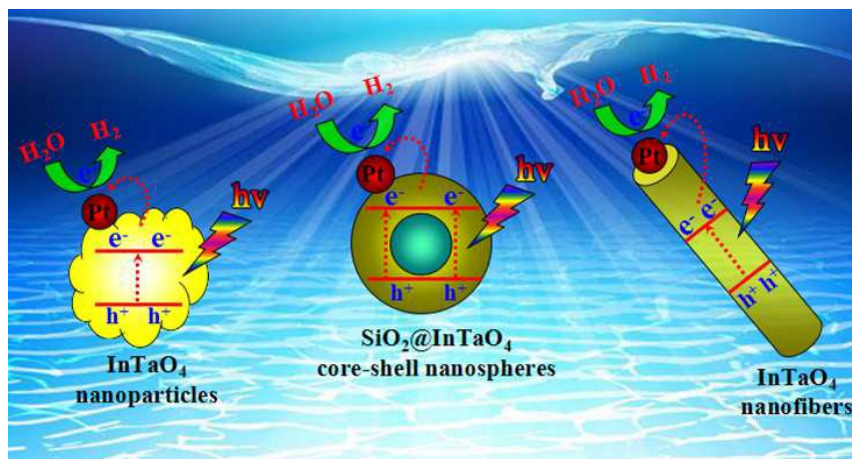
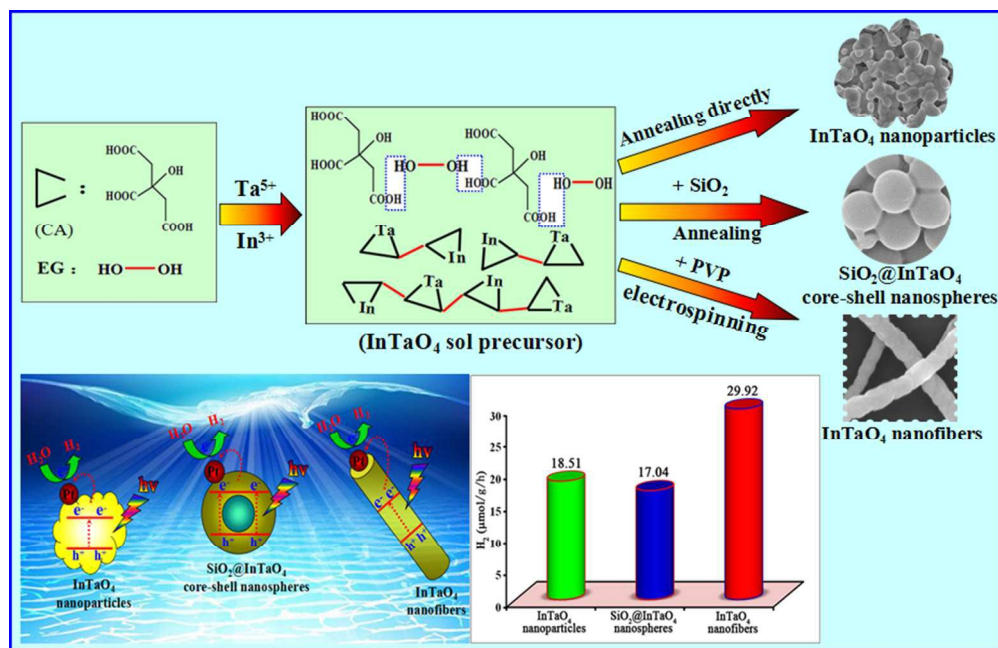


Fig. 6. The rate of hydrogen evolution over InTaO₄ nanoparticles, SiO₂@InTaO₄ core-shell nanospheres, and InTaO₄ nanofibers under simulated solar irradiation.



Scheme 2. Photocatalytic scheme of InTaO₄ nanoparticles, SiO₂@InTaO₄ core-shell nanospheres, and InTaO₄ nanofibers.



245x157mm (96 x 96 DPI)